ORIGINAL PAPER

Thermally enhanced shale gas recovery: microstructure characteristics of combusted shale

Yuan-Hao Cao[1] · Wei Chen[1] · Teng-Xi Wang[2] · Yin-Nan Yuan[1]

Abstract

Recently, thermal recovery technologies such as combustion have been studied for shale gas recovery. Thus, understanding of the microstructure of combusted shale is essential for evaluating the effects of thermal treatment on shale gas transport capacity. In this study, the effect of combustion on shale microstructure changes was investigated. Firstly, different-sized shale samples were combusted at 450 °C for 30 min. Afterward, shale microstructure properties including surface topographies, porosity and permeability of the raw and combusted shale samples were measured and compared. It was found that the pore volume and specific surface area increased after combustion, especially for small pulverized samples. According to surface topography obtained from atomic force microscope, more rough surfaces were obtained for the combusted shale due to larger pores and generation of thermal fractures caused by the removal of organic matter. Based on the mercury intrusion porosimetry measurements, the porosity of the shale samples increased from 2.79% to 5.32% after combustion. In addition, the permeability was greatly improved from 0.0019 to 0.6759 mD, with the effective tortuosity decreased from 1075.40 to 49.27. As a result, combustion treatment can significantly improve the gas transport capacity.

Keywords Shale · Combustion · Microstructure · Porosity · Permeability · Particle size

1 Introduction

Because of abundant reserves and low carbon emissions of shale gas, extraction of hydrocarbon products from shale reservoirs has attracted worldwide interests (Chen et al. 2017a; Huang and Zhao 2017). However, shale has extremely low permeability and complicated pore system, which is characterized by various pore types and wide pore size distributions (Sarkar et al. 2018). These characteristics significantly affect gas storage and flow transport behavior (Bai et al. 2019; Chen et al. 2016; Deng et al. 2016; Ji et al. 2016; Tian et al. 2013). Hence, a large-scale extraction of the shale gas from the tight shale matrix is challenging. Recently, the combustion treatment has been proposed for

shale gas recovery (Chapiro and Bruining 2015; Chen et al. 2017b). Combustion treatment not only provides energy for gas desorption from pore surfaces but also promotes the gas transport by improving the permeability (Chen et al. 2017b, 2018a, 2019c, d). However, pore system evolution during combustion process involves complicated physical and chemical processes. The knowledge in this area is still limited and needs further exploration.

Various classifications of pore types in shale have been proposed in previous studies (Desbois et al. 2009; Heath et al. 2011; Loucks et al. 2012; Pommer and Milliken 2015; Slatt and O'Brien 2011; Zhu et al. 2018). Based on pore size, shale pores could be divided into three types: micropore (< 2 nm), mesopore (2–50 nm) and macropore (> 50 nm) (Sing et al. 1985). Nanoscale gas transport mechanism and gas adsorption capacity in shale vary with different pore sizes and structures (Yu et al. 2017). The enlarged nanopores can lead to an increase in the conductivity of slippage flow and the contribution degree of slippage flow to the total gas transport capacity (Sun et al. 2019). In addition, the non-negligible gas adsorption and surface diffusion in the micropores and fine mesopores (< 10 nm) significantly affect the potential of the storage and transport of shale gas (Xiong

✉ Wei Chen
   timtamu@suda.edu.cn

1 School of Energy, Soochow University, Suzhou 215006, Jiangsu, China

2 Department of Mechanical Engineering, Texas A&M University, College Station 77840, USA

et al. 2017; Yu et al. 2017). Based on pore connectivity, shale pores can be divided into interparticle pores, intraparticle pores and organic pores (Katz and Arango 2018; Loucks et al. 2009). The low pore connectivity of shale also affected the gas transport (Hu et al. 2015). The pore connectivity is closely related to the type and shape of the nanopores. It was assumed that organic pores and interparticle pores have higher possibility to be interconnected than intraparticle pores (Loucks et al. 2012). It was also proposed that the porous floccules, microfractures and organic pores were more likely to contribute to permeability (Slatt and O'Brien 2011). Because of the importance of permeability to shale gas recovery, much attention was given to the contribution of microfractures (Yao et al. 2013; Zhu et al. 2018).

Three types of pore-throat systems were found in shale, including closed pores, pores with one throat and pores with multiple throats (Sarkar et al. 2018). A considerable fraction of gas transport may be restricted by these pore structures. Closed pores in shale have been studied due to their impacts on pore connectivity and permeability. Since the closed pores mainly exist in organic matter (Sun et al. 2018), the closed pores may be affected by combustion as a result of organic matter decomposition, which needs further investigation. The porosity changes after pulverization treatment had been proposed to explore the closed pore characteristics (Chen et al. 2018b). Therefore, different-sized shale particles should be investigated to make a more comprehensive analysis of the shale microstructure.

Thermal treatment has been found to greatly affect the shale microstructure. Since organic matter has a strong methane-adsorption capacity (Chen et al. 2019a; Song et al. 2018), the removal of organic matter may significantly affect the gas adsorption and transport in shale. It was found that the shale porosity was strongly related to the evolution of organic matter (Guo et al. 2017). The pyrolysis of kerogen may enlarge the pores with a corresponding increase in pore volume and specific surface area (Han et al. 2006). It was also found that the mean pore diameter of shale increased after combustion (Chen et al. 2017b). During combustion, the organic matter was decomposed, and thermal cracking hydrocarbon gases were generated. This process leads to a significantly increase in the internal pressure of shale (Chen et al. 2019b). The increased internal pressure would result in the change in gas transport mechanism in nanopores (Yu et al. 2018). However, because of the various pore types and complicated pore structure, the effect of thermal treatment on shale microstructure still needs more comprehensive analysis. Since the pore characteristics of combusted shale have not been well studied, it is necessary to study the changes in organic matter pores and other types of pores after combustion, as well as the porosity and permeability changes.

In this study, shale samples were first crushed and sieved to get five different-sized samples. Then, the samples were combusted at 450 °C for 30 min. The pore sizes of raw and combusted shale were then analyzed using low-temperature N_2 adsorption (LTNA). The porosity and permeability changes were investigated using mercury intrusion porosimetry (MIP) tests. The pore characteristics of different-sized samples were analyzed and compared to explore the effects of combustion on various pore structures of shale. Finally, the surface topographies of shale samples were observed using scanning electron microscopy (SEM) and atomic force microscope (AFM) to get a more comprehensive study.

2 Sample analysis

2.1 Shale sample preparation

In this study, the shale samples were collected from Wenjiaba in Zhina Coalfield, Guizhou Province, China, in a burial depth of 530–570 m. The Zhina Coalfield is located in the west of Guizhou Province, tectonically in the western portion of Yangtze Continental Block, which has abundant coal and shale resources (Li et al. 2017).

Before the experiments, the raw shale samples were first crushed and sieved using different screening standards corresponding to 0.71–1.00 mm (RS1), 0.355–0.450 mm (RS2), 0.088–0.150 mm (RS3), 0.045–0.063 mm (RS4) and 0–0.045 mm (RS5), shown in Fig. 1. These samples were then prepared for the combustion experiments.

According to the TGA–FTIR results of shale sample from Wenjiaba in previous studies (Chen et al. 2019d), the rapid weight loss occurred when the shale samples were heated up to 400 °C, and the weight loss rate was maximum at around 450 °C and 580 °C. Therefore, the temperatures 400 °C and 450 °C were selected to study structure characteristic changes. At the beginning, the tube furnace was preheated to a desired temperature. In the meantime, air was supplied to the tube furnace at a constant flow. Afterward, the samples (RS1–RS5) were inserted into the furnace and combusted at 450 °C for 30 min and the sample RS1 at 400 °C for 30 min. After the combustion experiment, the raw and combusted samples (RS1 to RS5 and CS1 to CS5) were subjected to LTNA tests. The raw and combusted samples RS1 and CS1 were selected for MIP and SEM tests, and the samples RS1 and CS6 were selected for AFM tests.

2.2 Shale properties

To analyze the shale properties, shale samples were sent to a commercial laboratory for property analysis including proximate analysis, ultimate analysis and vitrinite reflectance.

These analysis results are given in Table 1 (Chen et al. 2019d).

2.3 Pore characteristics of shale samples

In order to obtain pore characteristics of the shale samples, low-temperature N_2 adsorption measurements were performed using a Micromeritics TriStar II 3020 surface area analyzer. Before the measurements, all samples were dried and degassed at a constant temperature of 100 °C for 4 h to remove moisture and adsorbed gases. Then, about 0.2 g of these samples was analyzed exposed to N_2 at 77 K. The N_2 adsorption volume was measured with relative pressure (P/P_0) ranging from 0.050 to 0.995. The pore parameters such as pore volume, surface area and pore size distribution can be calculated using multiple adsorption theories such as Langmuir, Brunauer–Emmett–Teller (BET) and Barrett–Joyner–Halenda (BJH).

In this study, the raw and combusted samples with the particle size of 0.71–1.00 mm (RS1 and CS1) were sent to a commercial laboratory for the MIP test to measure the shale porosity and permeability. MIP tests were performed using a Micromeritics IV AutoPore 9500 Instrument, with the maximum pressure of 227.45 MPa. The shale samples RS1 and CS1 were dried and degassed prior to the tests. The porosity, permeability and effective tortuosity of the raw and combusted samples were investigated.

2.4 Morphology analyses of shale samples

The microstructure and morphology of the raw and combusted shale samples were analyzed using SEM and AFM imaging study. Before the experiments, in order to reduce the error of experimental results caused by heterogeneity of shale, the observation position was marked on the shale sample. The SEM equipment used (HITACHI SU8010) was operated under an acceleration voltage of 1 kV and a beam current of 10 µA. The scanning range of the AFM used (MFP-3D-BIO) was $90 \times 90 \times 15$ µm, with accuracy of 0.6 nm and height precision less than 0.03 nm.

3 Results and discussion

3.1 Shale properties

As shown in Table 1, the shale sample has a high ash content of 87.58%, and the total organic matter is around 10%, including 2.39% fixed carbon and 7.44% volatile matter. The high content of organic matter provides a large amount of potential adsorption sites for shale gas (Chen et al. 2018a). According to the kerogen-type descriptions, the kerogen type of these shale samples is dominated by Type II with the H/C atomic ratios about 1.07 and O/C atomic ratios about 0.145 (Jarvie 2015). The vitrinite reflectance (R_o) is 2.7%, which shows a relatively high thermal maturity, indicating that the shale was in the dry gas window (Jarvie 2015), while for high mature shale ($R_o = 2.7\%$) the amount of the dissolved gas would be ignored (Guo 2013).

Table 1 Proximate analysis, ultimate analysis and vitrinite reflectance of shale sample, adapted from Chen et al. (2019d)

Moisture, %	Ash, %	Volatile matter, %	Fixed carbon, %	Carbon, %	Oxygen, %	Hydrogen, %	Nitrogen, %	Sulfur, %	Vitrinite reflectance R_o, %
2.59	87.58	7.44	2.39	5.36	1.04	0.48	0.26	5.36	2.7
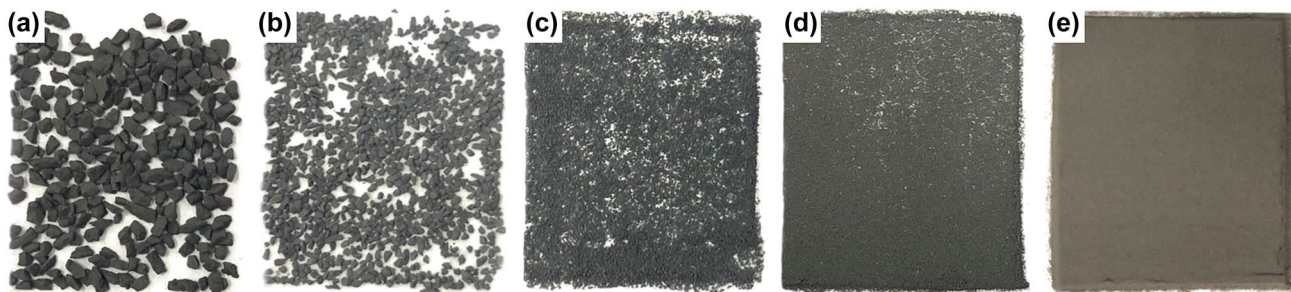
Fig. 1 Combusted shale samples with different particle sizes: **a** 0.710–1.000 mm, **b** 0.355–0.450 mm, **c** 0.088–0.150 mm, **d** 0.045–0.063 mm, **e** 0–0.045 mm

3.2 Low-temperature N_2 adsorption measurements

3.2.1 N_2 adsorption–desorption isotherms

According to IUPAC, six sorption isotherms (I to VI) and four types of hysteresis loops (H1 to H4) are commonly used to characterize the sorption behavior of porous materials (Sing et al. 1985). Figure 2 shows the N_2 adsorption–desorption isotherms of the shale samples. Although not showing a plateau at high P/P_0, these isotherms are all similar to the IUPAC type IV isotherms, indicating the presence of mesopores and macropores (Sing et al. 1985; Tian et al. 2013). The hysteresis loops of these isotherms all correspond to type H4, which are often associated with narrow slit-shaped pores (Liu et al. 2018; Lowell et al. 2004; Sing et al. 1985). It was found that the slit pore structure has a higher gas transport capacity than other pore structures such as circular pores (Yu et al. 2019). The lack of closure of the hysteresis loops at low relative pressure can also be found in previous studies (Chen et al. 2015, 2018b; Mastalerz et al. 2012), thought to be associated with the swelling of the porous structure or the irreversible uptake of molecules in pores (Sing et al. 1985).

The sample RS1 shown in Fig. 2a with the biggest particle size adsorbed the least amount of N_2 (0.99 cm^3/g), while the sample RS5 with the smallest particle size had the largest adsorption volume (14.35 cm^3/g). The N_2 adsorption capacity of the samples increased with the decrease in the particle size, indicating that the pulverization makes more pores accessible.

It is shown in Fig. 2b that the isotherms and hysteresis loops of the combusted shale samples were similar to raw samples. The amounts of adsorbed N_2 increased from CS1

(10.78 cm^3/g) to CS5 (26.96 cm^3/g), which were much larger compared with counterparts of raw shale particles. The increased adsorbed amount after combustion can be mainly attributed to the oxidization of organic matters, which can result in the enlargement of organic matter pores as well as the increases in pore volume and adsorbed surface area.

3.2.2 Pore volume

The pore volume distributions of micropores (< 2 nm), mesopores (2–50 nm) and macropores (> 50 nm) were also obtained from LTNA tests. The micropore volume was acquired using t-plot method, while the volume of mesopore and macropore (2–300 nm) was acquired using the BJH method.

The pore volume distribution given in Fig. 3 shows that the volumes of the three types of pores increased with the decrease in particle sizes of samples. The micropore volume increased from 0.64×10^{-3} cm^3/g (CS1) to 8.42×10^{-3} cm^3/g (CS5). The volumes of mesopores and macropores were also increased. The total pore volume increased from 16.65×10^{-3} cm^3/g (CS1) to 41.80×10^{-3} cm^3/g (CS5). In other words, the pore volume of the inaccessible pores which were exposed by crush reached up to 25.15×10^{-3} cm^3/g. Furthermore, the mesopores took up a large proportion in the total pore volume and had the largest increase compared with the other two types of pores, indicating that the mesopores had a great effect on the pore volume of shale.

As shown in Fig. 4, the pore volumes of different-sized shale particles including raw and combusted samples are compared. The pore volume of raw samples had the same trend with the combusted samples which was also increased with the particle size decreasing, from
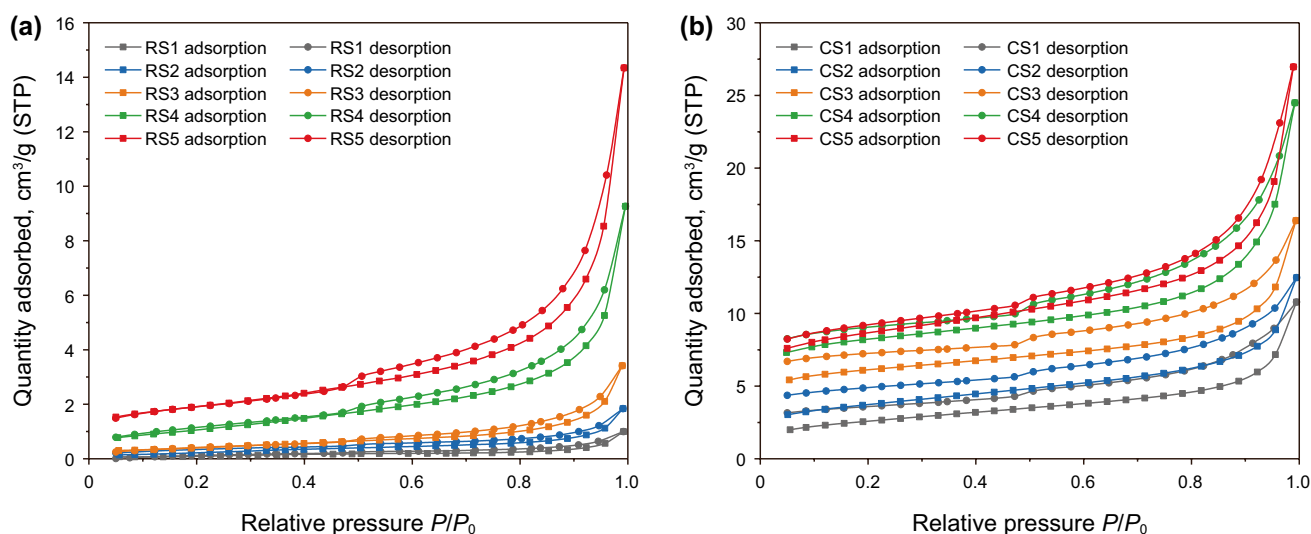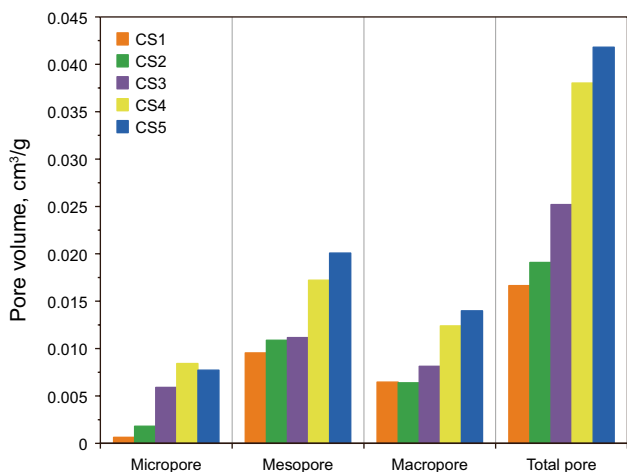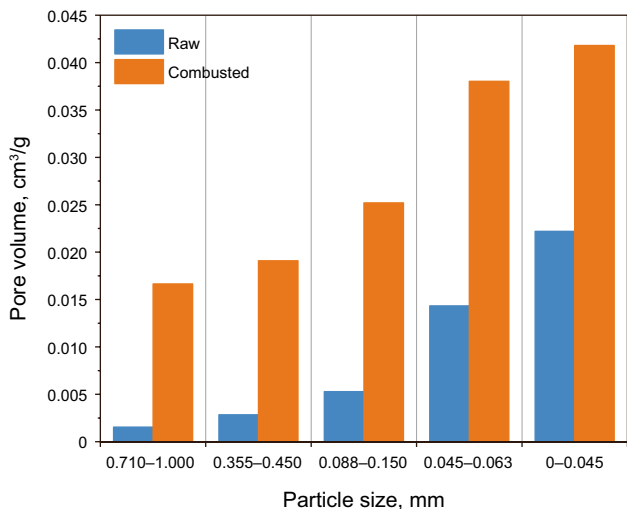

Fig. 2 N_2 adsorption and desorption isotherms of (**a**) raw and (**b**) combusted shale samples

Fig. 3 The volumes of micropores, mesopores, macropores and the total pores of the different-sized combusted samples based on *t*-plot method and BJH method

Fig. 4 The pore volumes of different-sized particles of raw and combusted shale samples based on *t*-plot method and BJH model

1.54×10^{-3} cm³/g (RS1) to 22.19×10^{-3} cm³/g (RS5). The increased pore volume of 20.65×10^{-3} cm³/g showed the volume of newly exposed pores. It was 4.5×10^{-3} cm³/g less than the amount in combusted samples. Moreover, raw sample of each size had much smaller pore volume than the combusted samples. This can be attributed to the combustion treatment which can further improve the porosity and pore connectivity of shale. Compared with pulverization, the combustion treatment can significantly improve the porosity of shale. It is interesting that the increased pore volumes after combustion were all around 20×10^{-3} cm³/g, which may reflect the amount of removed organic matter. This indicates that the effect of combustion on shale pores is mainly reflected in the removal of organic matter and the enlargement of organic pores.

3.2.3 Pore surface area

The surface area plays a key role in the adsorption of the shale gas. The change tendency of pore surface areas was similar to that of pore volume. The specific surface areas measured based on the BET method are given in Fig. 5. The specific surface areas of the combusted samples increased from 8.99 m²/g (CS1) to 27.91 m²/g (CS5) with decreasing particle size, while those of the raw samples from 0.4199 m²/g (RS1) to 6.5886 m²/g (RS5). The surface areas of raw and combusted samples all increased with the decrease in particle size because of the newly developed open pores by pulverization. It also can be seen that the specific surface areas significantly increased after combustion. Given that the specific surface area is mainly affected by smaller pores (Tian et al. 2013) and the micropores in shale are largely developed in organic matter (Li et al. 2016), the increase in specific surface area may be mainly attributed to the oxidization of organic matter by combustion. In the oxidization process, numerous small organic pores enlarged, respectively. However, there are also some studies that found that the specific surface areas of shale decreased after combustion. This may be due to the differences in sample properties and the oxidation degree of organic matter in shale.

3.2.4 Pore size distribution

The pore size distributions of raw and combusted shale samples were analyzed using BJH adsorption data and are given
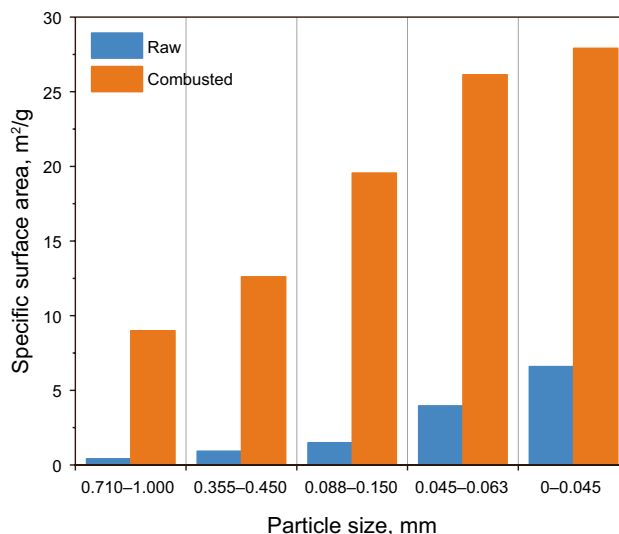
Fig. 5 The specific surface areas of shale samples based on BET method

in Fig. 6. After combustion, the pore volumes of micropores, mesopores and macropores were all increased, which means more flow transport channels were created. For high mature shale, micropores are well developed and hosted in organic matter (Tian et al. 2013; Yang et al. 2016). Under high-temperature combustion, a large amount of original closed micropores were reopened and the organic matters were decomposed, both of which resulted in the generation of significant micropores. The original stored gases in the closed pores became extractable. Besides, more mesopores and macropores were obtained due to the oxidization of organic matter. In micropores and mesopores, the gas flow was mainly slip flow or free molecular diffusion flow. As the pore size increased (Knudsen number Kn decreases), the gas transport shifted from diffusion flow to slip flow (Sun et al. 2019; Darabi et al. 2012). Thus, the gas transport capacity was improved.

3.3 The porosity and permeability of combusted shale

The porosity and permeability are the most important parameters to assess the gas transport in shale. Based on the results from MIP tests, it was found that the porosity of shale increased sharply from 2.79% to 5.32% after combustion at 450 °C. Furthermore, the permeability was greatly improved from 0.0019 to 0.6759 mD, with the effective tortuosity decreased from 1075.40 to 49.27.

Combustion resulted in not only the enlargement of open pores but also the generation of microfractures and the exposure of inaccessible pores. In addition, the decrease in effective tortuosity can also improve gas diffusion capacity. The diffusion coefficient can be given as (Veltzke and Thöming 2012):

$$D_k = \frac{1}{3}s\sqrt{\frac{8RT}{\pi M}} \tag{1}$$

where s is the pore diameter and M is molar mass.

The effective tortuosity τ is often related to effective diffusion coefficient (Sun et al. 2018):

$$\tau = \frac{D_k}{D_e} = \frac{1}{\phi}\left(\frac{L_e}{L}\right)^2 \tag{2}$$

where D_e is the effective diffusion coefficient in the porous media, m^2/s; ϕ is porosity, and L_e/L is the geometrical tortuosity.

Thus, the significant decrease in effective tortuosity τ indicates the improvement in effective diffusion coefficient based on Eqs. (1) and (2). This reveals that the gas diffusion potential inside shale pore systems was promoted after combustion treatment.

3.4 Pore-fracture morphology analyses based on SEM images

In order to study the microstructures of shale, the pore-fracture morphologies of the raw and combusted shale samples were observed using SEM. It is shown in Fig. 7a that the open pore networks in these samples mainly consisted of interparticle pores connected by microfractures. Numerous flocculated clay microfabrics are also shown in Fig. 7b, d. As a result of thermal cracking, the obvious microfractures that existed in combusted shale samples (Fig. 7c, d) can significantly improve the porosity and permeability of shale.

During the pulverization process, many closed pores were exposed to microfractures and the isolated intraparticle pores, such as pores in Fig. 7a, might be enlarged. In
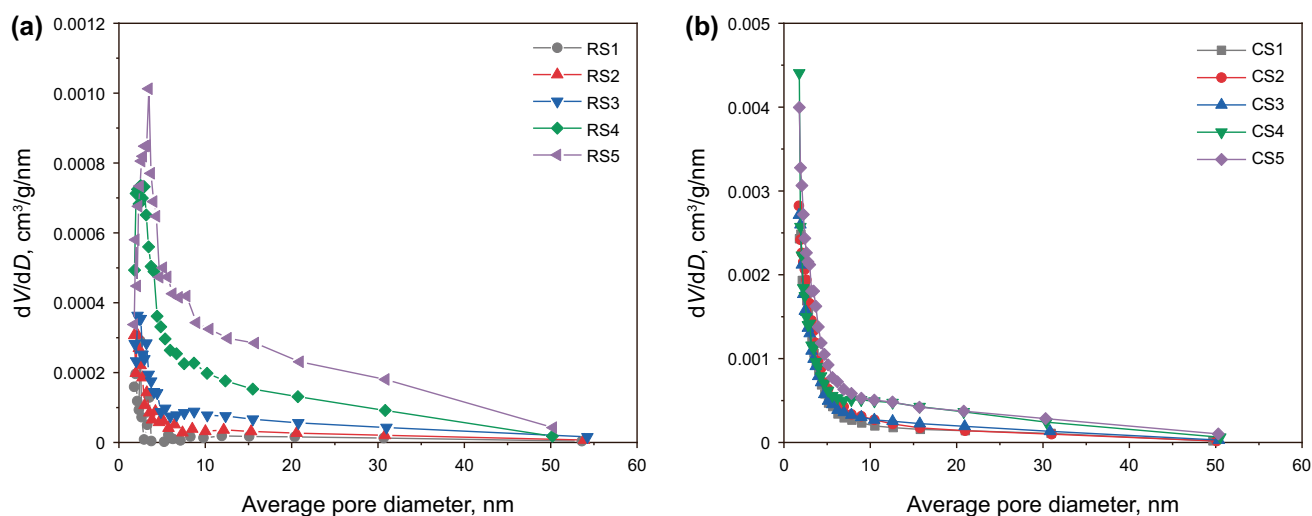

Fig. 6 Pore size distribution of (**a**) raw and (**b**) combusted shale samples from BJH adsorption data
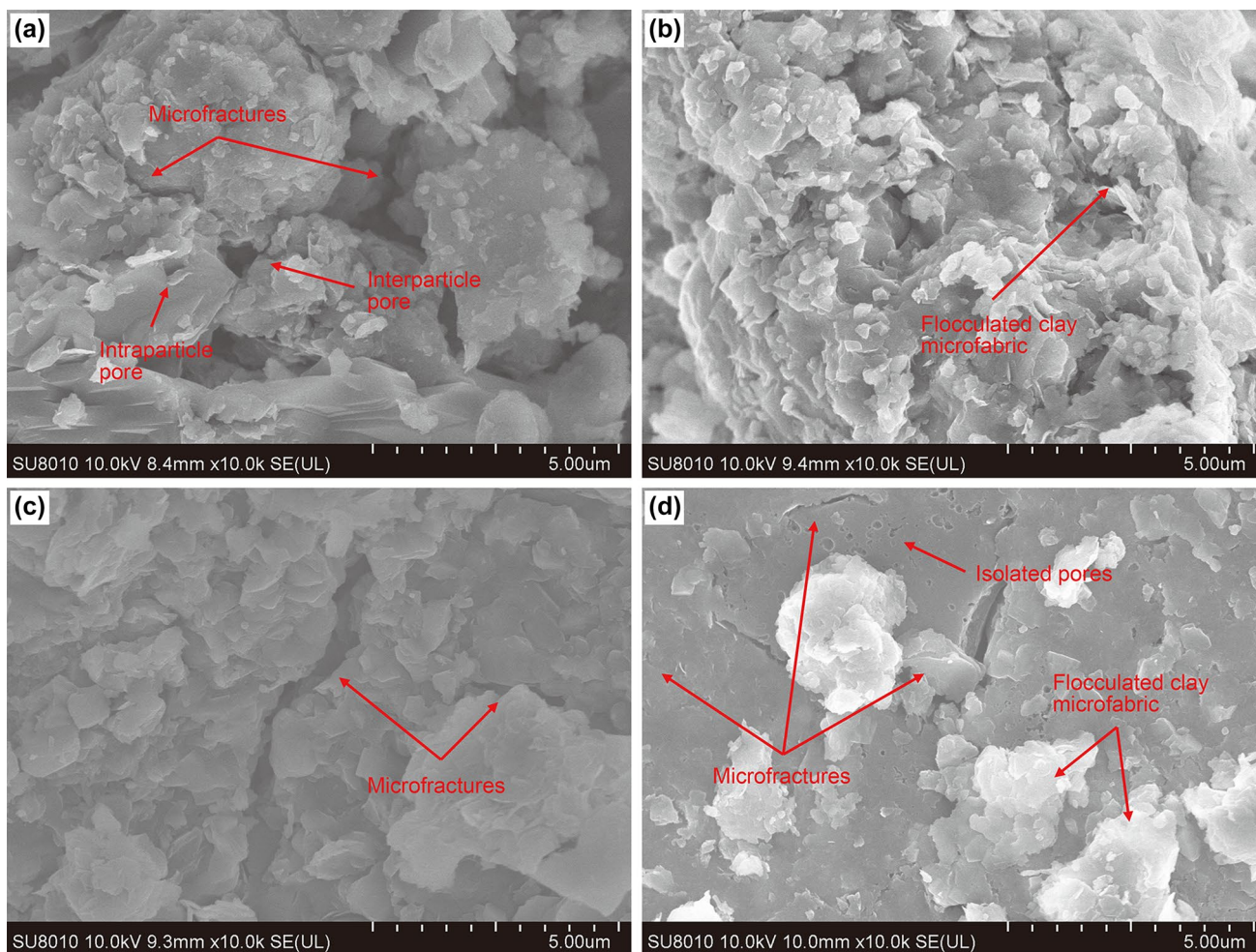
Fig. 7 SEM images of (**a**, **b**) raw and (**c**, **d**) combusted shale samples

addition, the microfractures were possibly generated. The original open pore networks could be developed due to the newly developed microfractures. This process reflects the enhancement of the pore connectivity.

3.5 AFM topography image of shale sample

During the combustion, some kerogen on the shale surface was removed and released as gas through oxidization (Chen et al. 2017b). To investigate the changes in shale morphology at the beginning of the rapid oxidization stage, the shale sample (RS1) was combusted at 400 °C for 30 min. The surface topographies of the shale samples before and after combustion (400 °C) were investigated using AFM. Using a sharp probe (a few nanometers in diameter) to measure the forces between the probe and the sample as a function of their mutual distance, nanoscale surface topography of shale surface (2D and 3D) was obtained, as shown in Fig. 8. The grooves (darker areas) in the grayscale images can be considered as nanopores

(Javadpour and Ettehadtavakkol 2015). The raw shale sample (Fig. 8a, b) had more even surfaces with about 1.4 μm in height and the maximum depth of 1.2 μm, while the combusted shale sample (Fig. 8c, d) had a more uneven surface with about 2.4 μm in height and 2.0 μm in depth, indicating deeper groove areas. This indicates that more organic matter was removed from the shale and resulted in larger pore volume. Moreover, the inaccessible pores blocked or restricted by organic matter might be connected to pore networks after combustion treatment.

It can be seen from Fig. 9a that the surface depth of raw shale is mainly between 0.5 and 1.5 μm. Moreover, the depth around 1.2 μm has the biggest percentage. After being combusted at 400 °C, the shale got wider surface depth distribution, ranging from 0.3 to 3.2 μm (Fig. 9b). Deeper surfaces were produced and were mainly in the range of 1.5 to 3.2 μm. As discussed before, the removal of organic matter resulted in bigger pore depth and areas. In other words, the porosity of the shale samples could be improved.
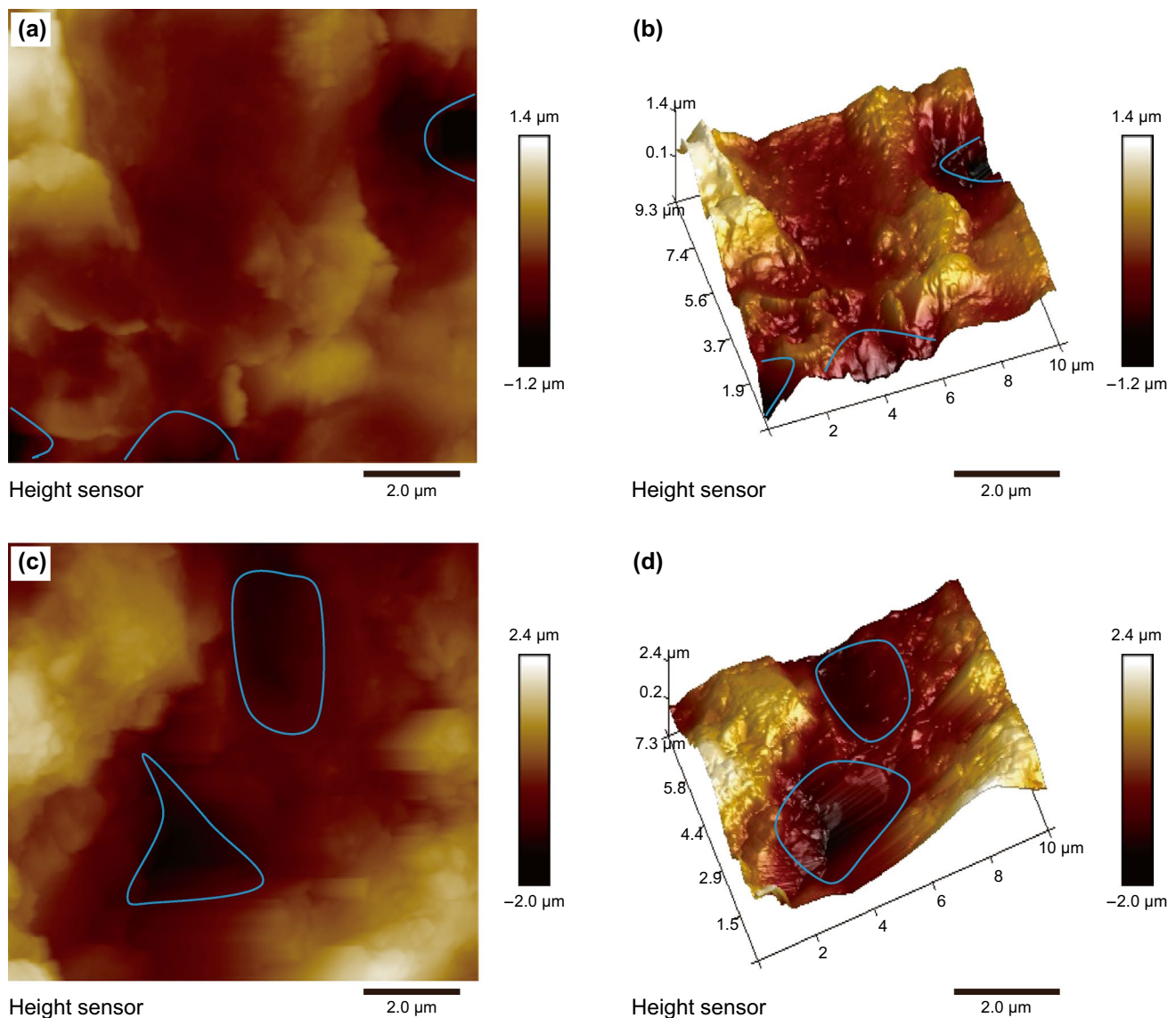
Fig. 8 2D and 3D height images of (**a, b**) raw and (**c, d**) combusted shale samples
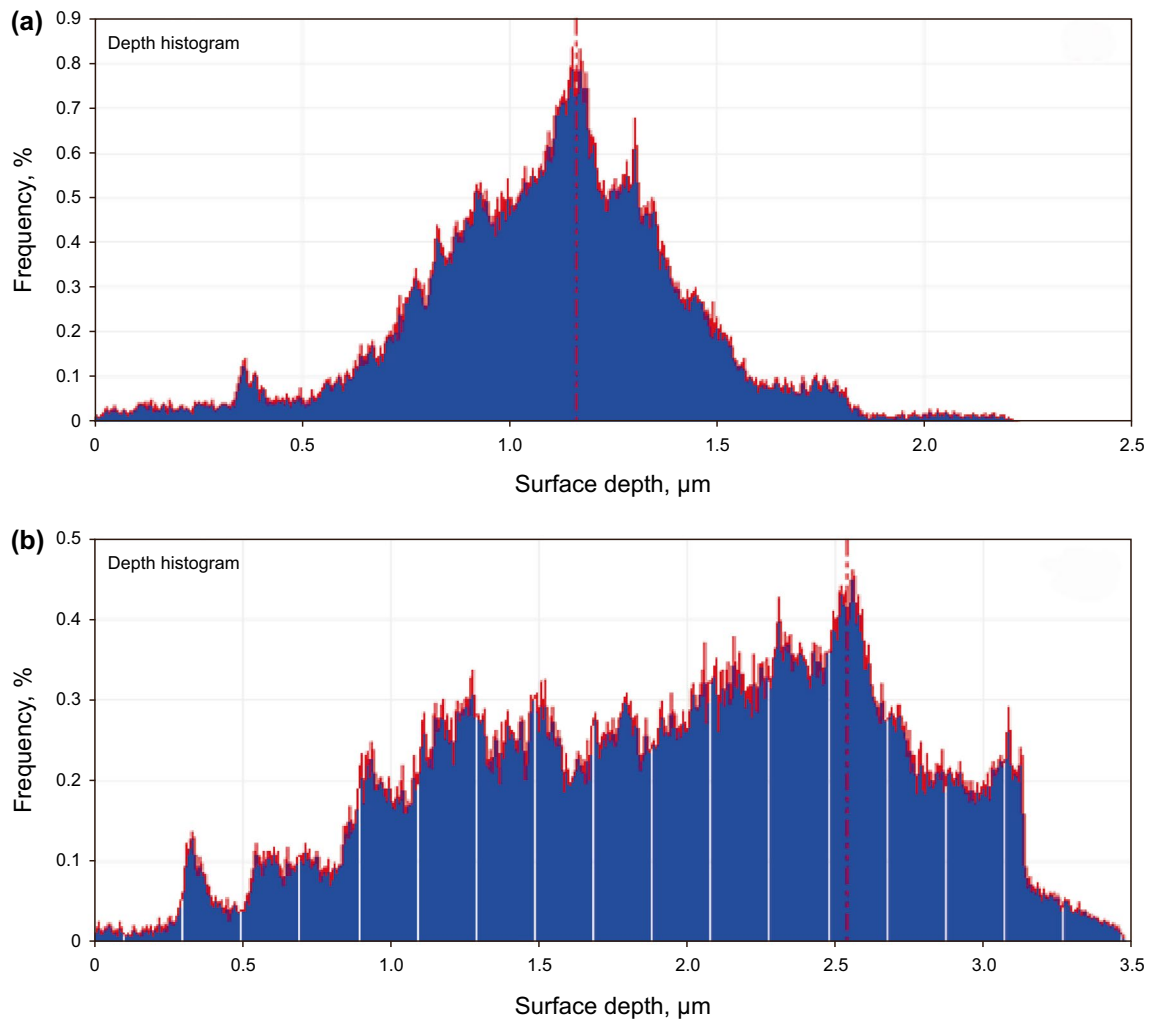
4 Conclusions

In this study, the effects of combustion treatment on shale physical and geochemical proprieties such as porosity and permeability changes were investigated. The main conclusions are listed as follows:

(1) The total organic matter content of the shale sample is around 10%, and the vitrinite reflectance value (R_o) was 2.7%. The kerogen type of the shale sample is dominated by Type II. These show that shale from Wenjiaba has a relatively high thermal maturity and rich organic matters.

(2) Combusted shale still had a wide pore size distribution. The porosity of shale increased after combustion.

More micropores were generated after combustion than mesopores and macropores. This is because many original closed micropores were reopened and nanopores were developed with the decomposition of organic matter. The volume of these pores is up to 20×10^{-3} cm^3/g.

(3) Combustion can significantly improve the gas transport capacity. Combustion treatment can lead to the removal of the organic matter and enlarged organic pores. Shale porosity can be further improved by combustion after pulverization, which increased from 2.79% to 5.32%. The permeability improved from 0.0019 to 0.6759 mD, and the effective tortuosity decreased from 1075.40 to 49.27.

Fig. 9 Depth histogram of (**a**) raw and (**b**) combusted shale samples

References

Bai J, Kang Y, Chen M, Liang L, You L, Li X. Investigation of multi-gas transport behavior in shales via a pressure pulse method. Chem Eng J. 2019;360:1667–77. https://doi.org/10.1016/j.cej.2018.10.197.

Chapiro G, Bruining J. Combustion enhance recovery of shale gas. J Pet Sci Eng. 2015;127:179–89. https://doi.org/10.1016/j.petrol.2015.01.036.

Chen Y, Wei L, Mastalerz M, Schimmelmann A. The effect of analytical particle size on gas adsorption porosimetry of shale. Int J Coal Geol. 2015;138:103–12. https://doi.org/10.1016/j.coal.2014.12.012.

Chen W, Lei Y, Chen Y, Sun J. Pyrolysis and combustion enhance recovery of gas for two china shale rocks. Energy Fuels. 2016;30(12):10298–305. https://doi.org/10.1021/acs.energyfuels.6b02274.

Chen L, Jiang Z, Liu K, Tan J, Gao F, Wang P. Pore structure characterization for organic-rich Lower Silurian shale in the Upper Yangtze Platform, South China: a possible mechanism for pore development. J Nat Gas Sci Eng. 2017a;46:1–15. https://doi.org/10.1016/j.jngse.2017.07.009.

Chen W, Lei Y, Ma L, Yang L. Experimental study of high temperature combustion for enhanced shale gas recovery. Energy Fuels. 2017b;31(9):10003–10. https://doi.org/10.1021/acs.energyfuels.7b00762.

Chen W, Zhou Y, Yang L, Zhao N, Lei Y. Experimental study of low-temperature combustion characteristics of shale rocks. Combust Flame. 2018a;194:285–95. https://doi.org/10.1016/j.combustflame.2018.04.033.

Chen Y, Qin Y, Wei C, Huang L, Shi Q, Wu C, et al. Porosity changes in progressively pulverized anthracite subsamples: implications for the study of closed pore distribution in coals. Fuel. 2018b;225:612–22. https://doi.org/10.1016/j.fuel.2018.03.164.

Chen F, Lu S, Ding X, Ju Y. Evaluation of the density and thickness of adsorbed methane in differently sized pores contributed by various components in a shale gas reservoir: a case study of the Longmaxi Shale in Southeast Chongqing, China. Chem Eng J. 2019a;367:123–38. https://doi.org/10.1016/j.cej.2019.02.105.

Chen W, Lei Y, Hua X. Flow transportation inside shale rocks at low-temperature combustion condition: a simple scaling law. Combust Flame. 2019b;199:114–21. https://doi.org/10.1016/j.combustflame.2018.10.022.

Chen W, Yang J, Chen Y, Lei Y, Sun J, Wang T. Flow transportation inside shale samples during low temperature combustion: the effect of desorption and pyrolysis. Fuel. 2019c;242:77–83. https://doi.org/10.1016/j.fuel.2018.12.110.

Chen W, Zhou Y, Yu W, Yang L. Experimental study of low-temperature shale combustion and pyrolysis under inert and noninert environments. SPE Prod Oper. 2019d. https://doi.org/10.2118/194507-PA **Preprint**.

Darabi H, Ettehad A, Javadpour F, Sepehrnoori K. Gas flow in ultra-tight shale strata. J Fluid Mech. 2012;710:641–58. https://doi.org/10.1017/jfm.2012.424.

Deng H, Hu X, Li HA, Luo B, Wang W. Improved pore-structure characterization in shale formations with FESEM technique. J Nat Gas Sci Eng. 2016;35:309–19. https://doi.org/10.1016/j.jngse.2016.08.063.

Desbois G, Urai JL, Kukla PA. Morphology of the pore space in claystones—evidence from BIB/FIB ion beam sectioning and cryo-SEM observations. eEarth. 2009;4(1):15–22.

Guo S. Experimental study on isothermal adsorption of methane gas on three shale samples from Upper Paleozoic strata of the Ordos Basin. J Pet Sci Eng. 2013;110:132–8. https://doi.org/10.1016/j.petrol.2013.08.048.

Guo H, Jia W, Peng P, Zeng J, He R. Evolution of organic matter and nanometer-scale pores in an artificially matured shale undergoing two distinct types of pyrolysis: a study of the Yanchang Shale with Type II kerogen. Org Geochem. 2017;105:56–66. https://doi.org/10.1016/j.orggeochem.2017.01.004.

Han X, Jiang X, Yu L, Cui Z. Change of pore structure of oil shale particles during combustion. Part 1. Evolution mechanism. Energy Fuels. 2006;20(6):2408–12. https://doi.org/10.1021/ef0603277.

Heath JE, Dewers TA, McPherson BJOL, Petrusak R, Chidsey TC, Rinehart AJ, et al. Pore networks in continental and marine mudstones: characteristics and controls on sealing behavior. Geosphere. 2011;7(2):429–54. https://doi.org/10.1130/ges00619.1.

Hu QH, Liu XG, Gao ZY, Liu SG, Zhou W, Hu WX. Pore structure and tracer migration behavior of typical American and Chinese shales. Pet Sci. 2015;12(4):651–63. https://doi.org/10.1007/s12182-015-0051-8.

Huang X, Zhao Y. Characterization of pore structure, gas adsorption, and spontaneous imbibition in shale gas reservoirs. J Pet Sci Eng. 2017;159:197–204. https://doi.org/10.1016/j.petrol.2017.09.010.

Jarvie DM. Geochemical assessment of unconventional shale gas resource systems. In: Rezaee R, editor. Fundamentals of gas shale reservoirs. 1st ed. New Jersey: Wiley; 2015. p. 47–69.

Javadpour F, Ettehadtavakkol A. Gas transport processes in shale. In: Rezaee R, editor. Fundamentals of gas shale reservoirs. 1st ed. New Jersey: Wiley; 2015. p. 245–66.

Ji W, Song Y, Jiang Z, Meng M, Liu Q, Chen L, et al. Fractal characteristics of nano-pores in the Lower Silurian Longmaxi shales from the Upper Yangtze Platform, south China. Mar Pet Geol. 2016;78:88–98. https://doi.org/10.1016/j.marpetgeo.2016.08.023.

Katz BJ, Arango I. Organic porosity: a geochemist's view of the current state of understanding. Org Geochem. 2018;123:1–16. https://doi.org/10.1016/j.orggeochem.2018.05.015.

Li T, Tian H, Chen J, Cheng L. Application of low pressure gas adsorption to the characterization of pore size distribution of shales: an example from Southeastern Chongqing area, China. J Nat Gas Geosci. 2016;1(3):221–30. https://doi.org/10.1016/j.jnggs.2016.07.001.

Li B, Zhuang X, Li J, Querol X, Font O, Moreno N. Enrichment and distribution of elements in the Late Permian coals from the Zhina Coalfield, Guizhou Province, Southwest China. Int J Coal Geol. 2017;171:111–29. https://doi.org/10.1016/j.coal.2017.01.003.

Liu K, Wang L, Ostadhassan M, Zou J, Bubach B, Rezaee R. Nanopore structure comparison between shale oil and shale gas: examples from the Bakken and Longmaxi Formations. Pet Sci. 2018;16(1):77–93. https://doi.org/10.1007/s12182-018-0277-3.

Loucks RG, Reed RM, Ruppel SC, Jarvie DM. Morphology, genesis, and distribution of nanometer-scale pores in siliceous mudstones of the Mississippian Barnett Shale. J Sediment Res. 2009;79(12):848–61. https://doi.org/10.2110/jsr.2009.092.

Loucks RG, Reed RM, Ruppel SC, Hammes U. Spectrum of pore types and networks in mudrocks and a descriptive classification for matrix-related mudrock pores. AAPG Bull. 2012;96(6):1071–98. https://doi.org/10.1306/08171111061.

Lowell S, Shields JE, Thomas MA, Thommes M. Characterization of porous solids and powders: surface area, pore size and density. Part Technol. 2004;16(9):1620.

Mastalerz M, He L, Melnichenko YB, Rupp JA. Porosity of coal and shale: insights from gas adsorption and SANS/USANS techniques. Energy Fuels. 2012;26(8):5109–20. https://doi.org/10.1021/ef300735t.

Pommer M, Milliken K. Pore types and pore-size distributions across thermal maturity, Eagle Ford Formation, southern Texas. AAPG Bull. 2015;99(09):1713–44. https://doi.org/10.1306/03051514151.

Sarkar P, Kumar A, Singh KH, Ghosh R, Singh TN. Pore system, microstructure and porosity characterization of Gondwana shale of Eastern India using laboratory experiment and watershed image segmentation algorithm. Mar Pet Geol. 2018;94:246–60. https://doi.org/10.1016/j.marpetgeo.2018.04.006.

Sing KSW, Everett DH, Haul RAW, Moscou L, Pierotti RA, Rouquerol J, et al. Reporting physisorption data for gas/solid systems with special reference to the determination of surface area and porosity. Pure Appl Chem. 1985;57:603–19.

Slatt RM, O'Brien NR. Pore types in the Barnett and Woodford gas shales: contribution to understanding gas storage and migration pathways in fine-grained rocks. AAPG Bull. 2011;95(12):2017–30. https://doi.org/10.1306/03301110145.

Song W, Yao B, Yao J, Li Y, Sun H, Yang Y, et al. Methane surface diffusion capacity in carbon-based capillary with application to organic-rich shale gas reservoir. Chem Eng J. 2018;352:644–54. https://doi.org/10.1016/j.cej.2018.07.050.

Sun M, Yu B, Hu Q, Yang R, Zhang Y, Li B, et al. Pore structure characterization of organic-rich Niutitang shale from China: small angle neutron scattering (SANS) study. Int J Coal Geol. 2018;186:115–25. https://doi.org/10.1016/j.coal.2017.12.006.

Sun F, Yao Y, Li G, Dong M. Transport behaviors of real gas mixture through nanopores of shale reservoir. J Pet Sci Eng. 2019;177:1134–41. https://doi.org/10.1016/j.petrol.2018.12.058.

Tian H, Pan L, Xiao X, Wilkins RWT, Meng Z, Huang B. A preliminary study on the pore characterization of Lower Silurian black shales in the Chuandong Thrust Fold Belt, southwestern China using low pressure N_2 adsorption and FE-SEM methods. Mar Pet Geol. 2013;48:8–19. https://doi.org/10.1016/j.marpetgeo.2013.07.008.

Veltzke T, Thöming J. An analytically predictive model for moderately rarefied gas flow. J Fluid Mech. 2012;698:406–22. https://doi.org/10.1017/jfm.2012.98.

Xiong J, Liu X, Liang L, Zeng Q. Adsorption of methane in organic-rich shale nanopores: an experimental and molecular simulation study. Fuel. 2017;200:299–315. https://doi.org/10.1016/j.fuel.2017.03.083.

Yang R, He S, Hu Q, Hu D, Zhang S, Yi J. Pore characterization and methane sorption capacity of over-mature organic-rich Wufeng and Longmaxi shales in the southeast Sichuan Basin, China. Mar Pet Geol. 2016;77:247–61. https://doi.org/10.1016/j.marpetgeo.2016.06.001.

Yao J, Sun H, Fan D, Wang C, Sun Z. Numerical simulation of gas transport mechanisms in tight shale gas reservoirs. Pet Sci. 2013;10(4):528–37. https://doi.org/10.1007/s12182-013-0304-3.

Yu H, Chen J, Zhu Y, Wang F, Wu H. Multiscale transport mechanism of shale gas in micro/nano-pores. Int J Heat Mass Transf. 2017;111:1172–80. https://doi.org/10.1016/j.ijheatmasstransfer.2017.04.050.

Yu H, Fan J, Chen J, Zhu Y, Wu H. Pressure-dependent transport characteristic of methane gas in slit nanopores. Int J Heat Mass Transf. 2018;123:657–67. https://doi.org/10.1016/j.ijheatmasstransfer.2018.03.003.

Yu H, Zhu Y, Jin X, Liu H, Wu H. Multiscale simulations of shale gas transport in micro/nano-porous shale matrix considering pore structure influence. J Nat Gas Sci Eng. 2019;64:28–40. https://doi.org/10.1016/j.jngse.2019.01.016.

Zhu H, Ju Y, Qi Y, Huang C, Zhang L. Impact of tectonism on pore type and pore structure evolution in organic-rich shale: implications for gas storage and migration pathways in naturally deformed rocks. Fuel. 2018;228:272–89. https://doi.org/10.1016/j.fuel.2018.04.137.